Natural hyperbolicity in layered hexagonal crystal structures

Ali Ebrahimian[1,*] and Reza Asgari[2,3,†]

[1]*School of Nano Science, Institute for Research in Fundamental Sciences (IPM), Tehran 19395-5531, Iran*

[2]*School of Physics, Institute for Research in Fundamental Sciences (IPM), Tehran 19395-5531, Iran*

[3]*ARC Centre of Excellence in Future Low-Energy Electronics Technologies, UNSW Node, Sydney 2052, Australia*

(Received 5 October 2020; revised 25 December 2020; accepted 11 January 2021; published 22 January 2021)

Discovering the physical requirements for meeting the indefinite permittivity in natural material, as well as proposing a new natural hyperbolic media, offer a possible route to significantly improving our knowledge and ability to confine and control light in optoelectronic devices. We demonstrate the hyperbolicity in a class of materials with hexagonal $P6/mmm$ and $P6_3/mmc$ layered crystal structures, and its physical origin is thoroughly investigated. By utilizing density functional theory and solving the Bethe-Salpeter equation, we find that the layered crystal structure and symmetry-imposed constraints in Li_3N give rise to an exceedingly strong anisotropy in optical responses along in- and out-of-plane directions of the crystals, making it a natural hyperbolic in a broad spectral range from the visible spectrum to the ultraviolet. More excitingly, the hyperbolicity relation to anisotropic interband absorption, in addition to the impressive dependency of the conduction band on the lattice constant along the out-of-plane direction, provide the hyperbolicity tunability in these hexagonal structures under strain, doping, and alloying. Our findings not only suggest a large family of real hexagonal compounds as a unique class of materials for realization of the highly tunable broadband hyperbolicity, but they also offer an approach to search for new hyperbolic materials.

DOI: 10.1103/PhysRevB.103.035425

I. INTRODUCTION

Because of the manipulation of relative permittivity through materials engineering, metamaterials have become a subject of intense interest in various science and engineering research communities aiming to conduct their interaction with electromagnetic and optical signals [1]. Relative permittivity, $\epsilon_1(\omega) + i\epsilon_2(\omega)$, is the main optical quantity that describes the interaction between matter and electromagnetic waves. In hyperbolic metamaterials, $\epsilon_1(\omega)$ exhibits different signs along different directions, revealing the extreme anisotropy of the electronic structure. Anisotropic optical materials exhibit numerous novel properties and potential applications, such as negative refraction [2,3], subwavelength imaging [4–6] in the far-field, and an optical nanoscale cavity [7,8].

Electronic structure anisotropy is typically achieved in artificially engineered metamaterials that have complicated nanofabrication requirements, the high degree of interface electron scattering, and the feature size of the components. Circumventing these limitations, natural hyperbolic materials provide an extended hyperbolic frequency window with low losses, high light confinement, and a larger photonic density of states [9–14]. Heretofore, several materials, such as graphite, MgB_2, cuprate, ruthenate, and tetradymite, have been predicted as natural hyperbolic materials [9,15–18], while experimentally they were observed only in a few of them, e.g., in MoO_3 surfaces [11,13], structured hexagonal boron nitride [12], and T_d -WTe_2 thin films [19]. Previous materials investigations revealed that the layered crystal structures exhibit excellent intrinsic out-of-plane optical anisotropy providing the required conditions for achieving natural hyperbolic materials [20–22].

In the same way, a recent study showed that the layered nature of group-I nitrides with hexagonal $P6/mmm$ (α-type) crystal structure gives rise to an exceedingly strong anisotropy in the electronic structure [23]. The α-Li_3N-type structure possesses a layered structure composed of alternating planes of hexagonal Li_2N and pure Li^+-ions with weak interactions along the stacking direction. It should be noted that a similar behavior has been also reported in its counterparts, namely the high-temperature superconductor MgB_2 and AlB_2 [24,25]. In particular, the weak Coulombic interactions between adjacent layers compared with interactions in a layer lead to a less dispersive valence-band maximum (VBM) along Γ-A. It enhances the anisotropy of the electronic structures, causing the highly anisotropic optical responses along the in- and out-of-plane directions of the crystals. Furthermore, the binary alkali pnictide A_3B (A = Li, Na; B = N, P, As, Sb, Bi) with hexagonal $P6_3/mmc$ (β-type) structure meets a similar layered structure and nearly flat bands along the Γ-A, which are responsible for the anisotropy of the electronic structure [26,27]. At this stage, we show via a thorough investigation of the electronic and optical properties of α-Li_3N that due to these anisotropic responses, materials with α- and β-type crystal structures belong to the rare class of natural hyperbolic materials. We emphasize that all the α- and β-type structures have qualitatively the same physics as α-Li_3N does (see the supplemental material [28]).

*aliebrahimian@ipm.ir

†asgari@ipm.ir

As a prominent member of this class, Li_3N has been studied extensively as a distinguished superionic conductor while its optical properties remain unexplored. Using first-principles calculations and the Bethe-Salpeter equation approach, we show that Li_3N is a natural hyperbolic in a broad spectral range from the visible to the ultraviolet spectra. Interestingly, it exhibits a type-II hyperbolic response in the lower and upper parts of the hyperbolic window, while in the middle one it exhibits a type-I hyperbolic response. We find that the hyperbolicity in Li_3N is related to anisotropic interband absorption between the valence and conduction bands imposed by symmetry constraints and transition selection rules.

As a standard feature of this new class of natural hyperbolic materials [22,25,26], the valence and conduction band gap of Li_3N is highly impressionable and susceptible to the lattice constant c. These unique conditions provide the possibility of hyperbolicity tunability in Li_3N with strain, doping, and alloying. In fact, our calculations show that the hyperbolic window of Li_3N and the relative intensity of the subdiffraction and diffraction-limited waves in transmission through Li_3N can be efficiently tuned by applying strain along the z-axis and doping in addition to using its ternary compounds such as $Li_2K(Na)N$. Although Li_3N and $Li_2K(Na)N$ possess the same structure, the larger ionic radius of K(Na) leads to band crossing along the z-direction [23], which extends the hyperbolic window in the visible regime; this is highly desirable in light device applications. In addition to Li_3N and the related alloys, the anisotropic electronic structure of α- and β-type compounds gives rise to both type-I and type-II hyperbolic frequency windows, as well offering hexagonal $P6/mmm$ and $P6_3/mmc$ layered structures as a unique class of materials for realization of the highly tunable broadband hyperbolicity and relevant device applications.

The structure of the paper is as follows. In Sec. II, we briefly introduce the simulation methods. Section III is devoted to the numerical results of the study, focusing on the electronic and optical properties of the α-Li_3N crystal structure. Finally, we summarize our results in Sec. IV.

II. THEORETICAL AND COMPUTATIONAL METHODS

The electronic and linear optical properties of the insulator crystal structures (e.g., Li_3N) are calculated in the framework of density functional theory (DFT) and many-body perturbation theory. DFT is based on the accurate all-electron full-potential linearized augmented plane wave (FP-LAPW) method as implemented in EXCITING code [29]. Ground-state properties are calculated using the hybrid density functional (HSE06) [30,31] in addition to the PBE-type [32] generalized gradient approximation functional to satisfy the high-accuracy requirements. The hole doping induced in α-Li_3N is simulated by shifting the Fermi level downward according to a standard rigid-band model. A $20 \times 20 \times 20$ Monkhorst-pack k-point mesh is properly used in the computations. For Li_3N, the optical spectra are obtained by solving the Bethe-Salpeter equation (BSE) [33] and the equation of motion of the two-particle Green's function [34,35]. The matrix eigenvalue form of the BSE is thus given by [36–39]

$$\sum_{v'c'k'} \mathcal{H}^{\mathrm{BSE}}_{vck,v'c'k'} A^{\lambda}_{v'c'k'} = E^{\lambda} A^{\lambda}_{vck}, \tag{1}$$

where v, c, and k indicate the valence band, conduction band, and k-points in the reciprocal space, respectively. Eigenvalues E^{λ} and eigenvectors A^{λ}_{vck} represent the excitation energy of the jth-correlated electron-hole pair and the coupling coefficients used to construct the exciton wave function, respectively. In the Tamm-Dancoff approximation, the effective two-particle Hamiltonian for a spin-degenerate system is given by

$$\mathcal{H}^{\mathrm{BSE}} = \mathcal{H}^{\mathrm{diag}} + 2\mathcal{H}^{x} + \mathcal{H}^{d}, \tag{2}$$

where the kinetic term $\mathcal{H}^{\mathrm{diag}}$ is determined from vertical transitions between noninteracting quasiparticle energy, and it corresponds to the independent-particle approximation. The screened Coulomb interaction $\mathcal{H}^{d}$ and the bare electron-hole exchange $\mathcal{H}^{x}$ are responsible for the formation of bound excitons. Having calculated the eigenvalues and eigenvectors of the BSE, the long-wavelength limit of the imaginary part of the dielectric function $\epsilon_{\mathrm{ii}}(\omega)$ is given by [36,39,40]

$$\mathrm{Im}\epsilon_{ii}(\omega) = \frac{8\pi^2}{\Omega} \sum_{\lambda} |t_{\lambda}|^2 \delta(\omega - E^{\lambda}), \tag{3}$$

$$t_{\lambda} = \sum_{vck} A^{\lambda}_{vck} \frac{\langle vk|\hat{p}|ck\rangle}{\varepsilon^{c}_{\mathbf{k}} - \varepsilon^{v}_{\mathbf{k}}}, \tag{4}$$

where $\varepsilon^{l}_{\mathbf{k}}$ with $l = c, v$ is the eigenvalue of the Kohn-Sham (KS) equation. The imaginary part of the DFT dielectric function shows the excitations in the system. The optical properties of semimetal structures such as doped Li_3N, Li_2KN, and Na_3N are considered using time-dependent density-functional theory (TDDFT) [41]. The inverse dielectric matrix ϵ is related to the susceptibility χ (Refs. [36,42]) by the relation $\epsilon^{-1}(q,\omega) = 1 + v(q)\chi(q,\omega)$, where $v(q)$ is the bare Coulomb potential. In TDDFT, the susceptibility $\chi(q,\omega)$ is obtained by making use of the linear response to TDDFT through the solution of the Dyson equation;

$$\chi(q,\omega) = \chi_0(q,\omega) + \chi_0(q,\omega)[v(q) + f_{\mathrm{xc}}(q)]\chi(q,\omega), \tag{5}$$

where $\chi_0(q,\omega)$ is the KS susceptibility expressed in terms of the KS eigenvalues and eigenfunctions, while $f_{\mathrm{xc}}(q)$ is the exchange-correlation kernel, for which we make use of the adiabatic local-density approximation (ALDA). The neglect of the $f_{\mathrm{xc}}(q)$ term corresponds to the random-phase approximation (RPA) [36]. The macroscopic dielectric function ϵ_M is therefore defined as

$$\epsilon_M(\mathbf{q}',\omega) = \lim_{q\to 0} \frac{1}{\epsilon^{-1}_{\mathbf{G}=\mathbf{0},\mathbf{G}'=\mathbf{0}}(\mathbf{q},\omega)}, \tag{6}$$

where $\mathbf{q}' = \mathbf{q} + \mathbf{G}$, and $\mathbf{q}$ represents the momenta inside the first Brillouin zone.

III. NUMERICAL RESULTS AND DISCUSSIONS

Lithium nitrite (α-Li_3N) crystallizes in the hexagonal $P6/mmm$ structure (α-Li_3N-type crystal structure) as shown in Fig. 1. The α-Li_3N structure possesses a layered structure

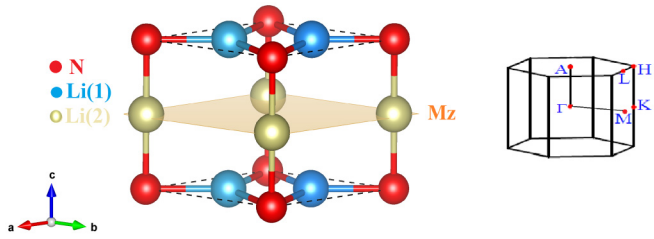

FIG. 1. The crystal structure (left panel) and the first Brillouin zone (right panel) of α-Li_3N with $P6/mmm$ symmetry. The mirror reflection plane is shown by M_z.

composed of alternating planes of the hexagonal Li_2N and pure Li^+-ions. In the Li_2N layers, each N (0, 0, 0) is at the center of a symmetrical hexagon formed by the six neighboring Li-ions (1/3, 2/3, 0) and (2/3, 1/3, 0) in units of lattice vectors. From now on, these Li atoms are denoted as Li(1), and the Li atom above the N atoms is denoted as Li(2). In this structure, the three lithium atoms donate their $2s$ electrons to the nitrogen, resulting in Li^+-ions and an N^{3-}-ion. For the Li_3N crystal structure, we obtain the lattice constants $a = b = 3.648$ and $c = 3.885$ Å, which are completely consistent with the ones reported in experiment [43–45].

The calculated orbital resolved band structure of Li_3N shows that the conduction-band minimum (CBM) around the Γ point is parabolic and mainly contributed by Li-s orbital while the valence-band maximum (VBM) along the Γ-A is a doubly degenerate band and mostly composed of N-p orbital. The weak interactions along the z direction lead to a less dispersive p_z VBM along the Γ-A and enhances the anisotropy of the electronic structures. This is the common feature of the α- and β-type crystals and response structure for the anisotropic optical properties.

As this novel natural hyperbolic class of materials contains also the semimetals with a Dirac node along the Γ-A, we depict the band structure of Na_3N as a semimetal member example in Fig. 2, providing a general overview of these electronic structures. In spite of the crystal structure similarity between Na_3N and Li_3N, as shown in Fig. 2, the CBM crosses the doubly degenerate VBM along the Γ-A generating a triply degenerate nodal point (TDNP). However, due to the similarities of the optical properties of Li_3N and Na_3N, we focus on the Li_3N structure. The results for Na_3N and some other members are given in the supplemental material [28]. In Li_3N, the PBE gap is 1.04 eV while the HSE06 gap is 2.12 eV, otherwise the band structures calculated by HSE06 are remarkably similar to those obtained within the PBE in the vicinity of the Fermi energy [see Fig. 2(a)]. The dielectric tensor of the hexagonal Li_3N is diagonal and retains two independent components: $\epsilon_{xx} = \epsilon_{yy}$ parallel to the Li_2N plane (in-plane), and ϵ_{zz} perpendicular to the Li_2N plane (out-of-plane).

The BSE (RPA) computed optical spectra of Li_3N are illustrated in Fig. 3. These calculations are performed by including the HSE06 correction to the PBE one. In a general comparison, the optical spectra of both $\mathrm{Im}\epsilon_{ii}$ and $\mathrm{Re}\epsilon_{ii}$ show considerable anisotropy between the in-plane and out-of-plane components with distinct resonances in various directions. The polarization dependence of the optical absorption originates from the structural anisotropy of Li_3N. In fact, the symmetry and space orientation of the valence and conduction bands would impose constraints on the optical transition selection rules [46], causing the polarization dependence of the optical absorption. The strength of the interband transition contribution to $\mathrm{Im}\epsilon_{ii}$ is proportional to the product of the joint density of states (JDOS) and the electric dipole transition moment matrix $\langle\psi_v|\hat{r}|\psi_c\rangle$, where ψ_v and ψ_c are the wave functions of the valence and conduction bands, respectively, and r is the position operator.

As the VBM is mainly composed of N-p orbital and the CBM is constructed from Li-s orbital, the electric dipole transition moment matrix is $\langle s|\hat{r}|p\rangle$. The nonzero elements and the electric dipole transition are determined by the optical selection rules. At the Γ point, the parity selection rule is fulfilled due to the opposite parities of the VBM and CBM. As the crystal structure has a mirror symmetry, $R_z = \sigma_z$, the VBM and CBM have the same eigenvalues with respect to the mirror reflection operation R_z at the Γ point. Therefore, at the Γ point the electric dipole transition is symmetry-allowed for the

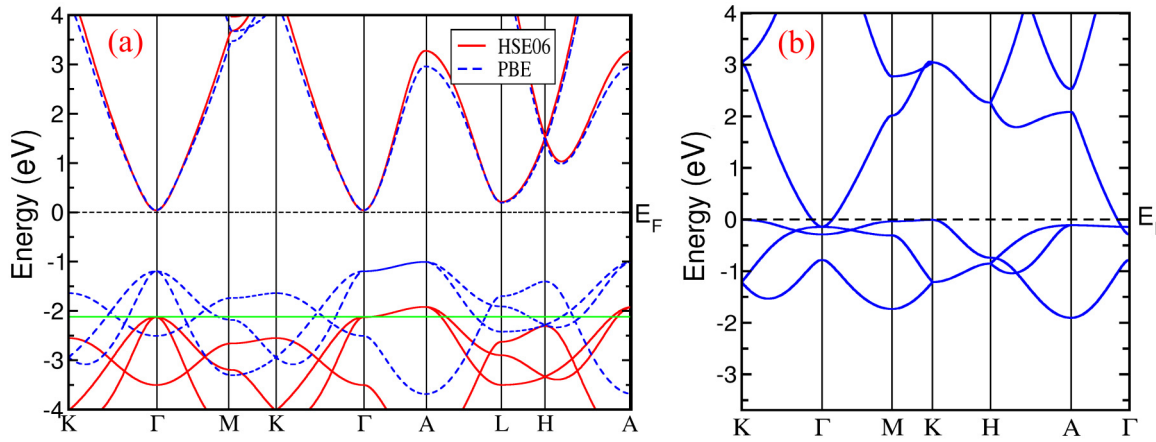

FIG. 2. The calculated bulk electronic band structure of (a) Li_3N and (b) Na_3N (in PBE). The value of the Fermi energy for 0.1 holes/u.c. is shown by a green solid line. The PBE gap of Li_3N is 1.04 eV while the gap is 2.12 eV within the HSE06. Other than the band-gap value, the structures calculated by HSE06 are remarkably similar to those obtained within the PBE in the vicinity of the Fermi energy.

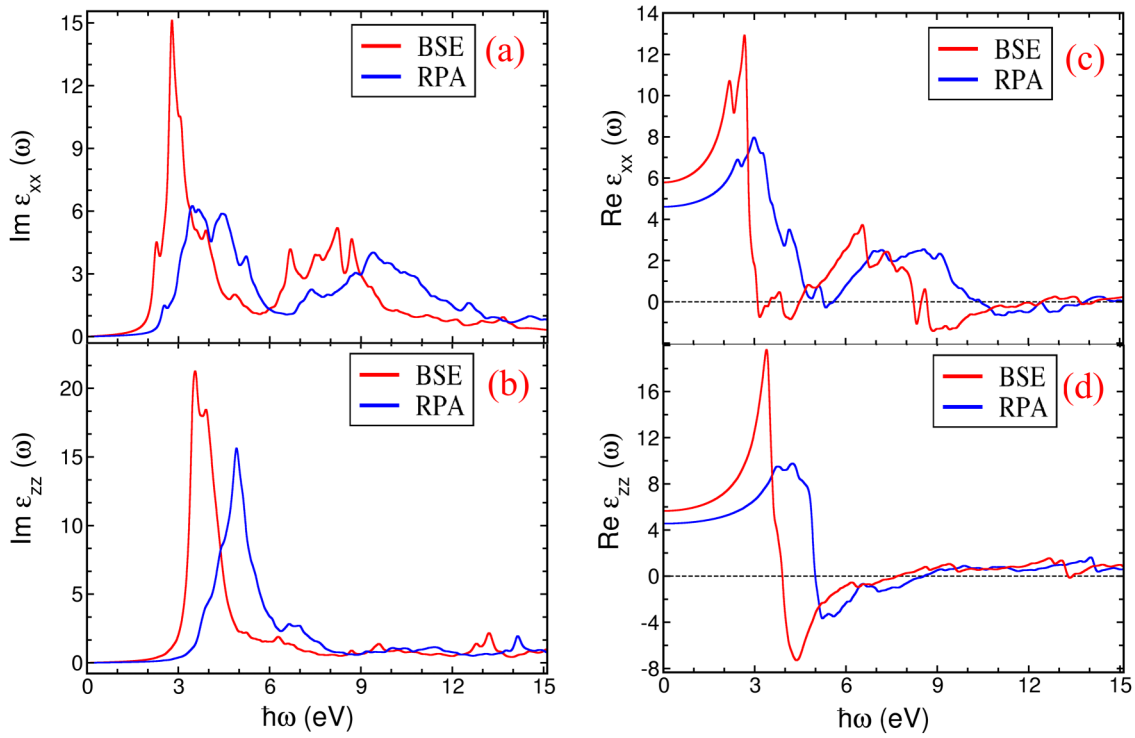

FIG. 3. The imaginary (a,b) and real (c,d) parts of the in-plane (top) and the out-of-plane (bottom) components of the macroscopic dielectric function Li_3N. The optical spectra of both $Im\epsilon_{ii}(\omega)$ and $Re\epsilon_{ii}(\omega)$ show considerable anisotropy between the in-plane and out-of-plane components with distinct resonances in various directions. The polarization dependence originates from the structural anisotropy of Li_3N. The BSE results are qualitatively different from those obtained within the RPA, especially in the lower part of the absorption. Moreover, the static dielectric constants along the in-plane and out-of-plane are 5.78 and 5.64 for Li_3N, respectively.

in-plane polarized light, while the transition in the out-of-plane direction is symmetry-forbidden under the mirror symmetry R_z. These symmetry constraints are responsible for an anisotropy between the in-plane and out-of-plane components of the dielectric tensors. The $Im\epsilon_{xx}$ has two main structures above 2 and 6 eV, while the $Im\epsilon_{zz}$ has one structure above 2 eV and decays more rapidly. As a result, the $Re\epsilon_{xx}$ oscillates between positive and negative values providing the required conditions for achieving a hyperbolic regime. Interestingly, Li_3N is transparent in most parts of the UV spectrum for the out-of-plane polarization direction. As shown in Fig. 3, the BSE results are qualitatively different from those obtained within the RPA, especially in the lower part of the absorption where the absorption onset is dominated by two intense peaks formed by bound excitons with large oscillator strengths. The analysis of the k-space distribution of the exciton weights shows that the first excitation originates from the VBM to the conduction band at the Γ point where the lowest-energy excitation is produced by the transition between the highest occupied band and the lowest-unoccupied band at the Γ point. The next excitations are mainly constituted by transitions between the first (second) highest occupied band and the lowest unoccupied band along the path Γ-A (Γ-K), close to the Γ point. Moreover, the static dielectric constants along the in-plane and out-of-plane are 5.78 and 5.64 for Li_3N, respectively. In considering the $Re\epsilon_{ii}$ of Li_3N, Figs. 3(c) and 3(d) show the negative values of the out-of-plane component of the real part of the dielectric function only from 3.94 up to 7.66 eV, which correspond to a high reflectivity region. Most excitingly, the in-plane component of $Re\epsilon_{ii}$ is mostly positive in this region, while it goes through a high reflectivity region outside of the region. As the in-plane and out-of-plane components of $Re\epsilon_{ii}$ cross zero at different frequencies, Li_3N fulfills the necessary conditions for type-I ($Re\epsilon_{xx} > 0$ and $Re\epsilon_{zz} < 0$) and -II ($Re\epsilon_{xx} < 0$ and $Re\epsilon_{zz} > 0$) indefinite permittivity media.

There are three clear type-II hyperbolic frequency regimes in the visible region (from 3.1 to 3.54 eV) and ultraviolet (UV) regime, including a narrow (from 8.23 to 8.5 eV) and a wide (from 8.67 to 12.48 eV) window as shown in Fig. 4(a). The wide type-I hyperbolic frequency regime is located between 4.51 and 7.66 eV. The type-I hyperbolic window supports propagating diffraction-limited and subdiffraction waves, while the type-II hyperbolic region only supports the latter. The relative intensity of the subdiffraction and diffraction-limited waves in transmission through Li_3N can be tuned by modifying the type of hyperbolic window providing a unique platform to the definitive experimental study of exotic phenomena such as the anti-cutoff [47]. An ideal hyperbolic material should be nearly lossless in the hyperbolic window.

We show, on the other hand, the energy loss function of Li_3N in Fig. 4(b). The energy loss function, $L(\epsilon(q,\omega)) = Im(-1/\epsilon(q,\omega))$, which determined the energy loss of a fast electron moving across a medium, is a complicated mixture of interband transitions and plasmons. Interband transition peaks are related to the peaks of $Im\epsilon_{ii}$, while the plasmon peaks correspond to zeros of the $Re\epsilon_{ii}$. The plasmon peak of the loss function is larger if $Re\epsilon_{ii}$ is zero and $Im\epsilon_{ii}$ is a significantly

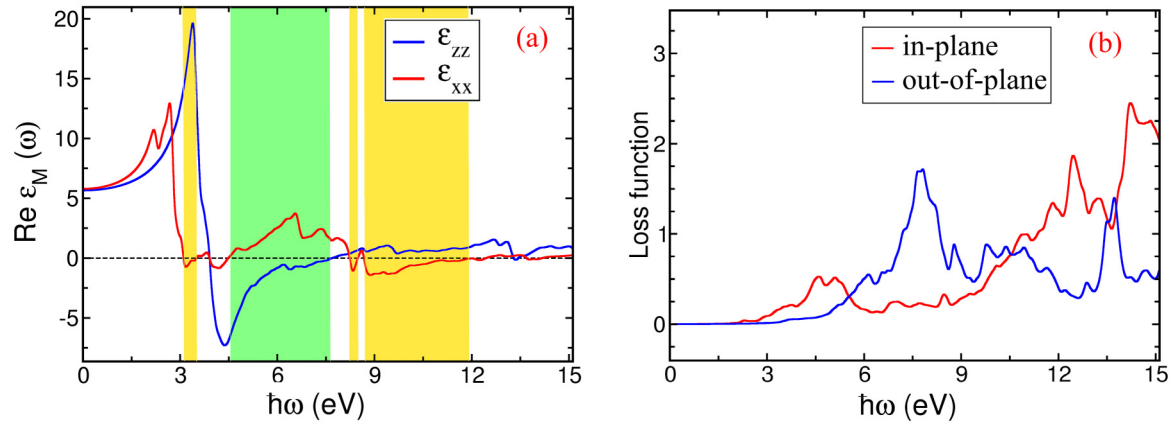

FIG. 4. (a) The real part of the dielectric tensor and (b) the energy loss function to in-plane (x-polarized) and out-of-plane (z-polarized) incident light for Li_3N. The spectral regions for type-I and -II hyperbolicity are marked with a green and yellow background, respectively. Three type-II hyperbolic frequency regimes are in the visible region (from 3.1 to 3.54 eV) and the ultraviolet (UV) region, including a narrow (from 8.23 to 8.5 eV) and a wide (from 8.67 to 12.48 eV) window. Interband transition peaks in panel (b) are related to the peaks of $\mathrm{Im}\epsilon_{ii}(\omega)$, while the plasmon peaks correspond to zeros of $\mathrm{Re}\epsilon_{ii}$. Notice that the plasmon excitation is located out of the hyperbolic windows.

small value. As shown in Fig. 4(b), both components of the loss function show negligible values in the entire hyperbolic energy window except a broad plasmon peak with a small intensity above 7.5 eV. This plasmon excitation is actually located out of the hyperbolic windows. Therefore, Li_3N is a low loss in hyperbolic frequency regimes making it an ideal natural hyperbolic material. The origins of the hyperbolic response regimes can be detected by considering the optical transitions between the valence and conduction bands in the hyperbolicity windows, shown in the electronic band structure in Fig. 3.

Due to the Kramers-Kronig relation [48] between the real and imaginary parts of the dielectric function, the high oscillator strength resonances of $\mathrm{Im}\epsilon_{xx}$ and $\mathrm{Im}\epsilon_{zz}$ at 2.8 and 3.7 eV are responsible for the negative permittivity in $\mathrm{Re}\epsilon_{xx}$ and $\mathrm{Re}\epsilon_{zz}$ at 3.1 and 3.9 eV in Fig. 4(a). These intense peaks in $\mathrm{Im}\epsilon_{xx}$ and $\mathrm{Im}\epsilon_{zz}$ are related to the interband transitions between the valence and conduction bands along Γ-A and L-A (see Fig. 2). The band structure of the system determines the occupied and unoccupied bands nearly parallel to each other in these domains, and therefore they have the same dispersions, resulting in a constant energy difference between the conduction and valence bands [$|\nabla_{\mathbf{k}}(E_c - E_v)| = 0$] [49]. As the JDOS can be expressed in terms of $|\nabla_{\mathbf{k}}(E_c - E_v)|$ [49],

$$\frac{1}{2\pi^2}\int \frac{dS_k}{|\nabla_{\mathbf{k}}(E_c - E_v)|}, \tag{7}$$

where S_k is the constant energy surface defined by $E_c - E_v =$ const, thereby the JDOS and absorption are significantly large along the Γ-A and L-A directions.

As before, the polarization dependence of the negative permittivity window (absorption) along the Γ-A and L-A directions is dictated by symmetry constraints and transition selection rules. The point groups along the high-symmetry lines Γ-A and L-A are D_{6h} and C_{2v}, which have a horizontal mirror plane σ_d ($R_z = \sigma_z$) and a vertical mirror plane σ_v, respectively. The VBM and CBM have the same eigenvalues with respect to the mirror reflection operation R_z along the Γ-A direction, while they maintain the same parity with respect to the vertical mirror plane σ_v along L-A. These constraints make the z-polarized transitions (x-polarized transitions) forbidden along Γ-A (L-A), causing the strong anisotropic dielectric tensors that represent the required condition for hyperbolicity.

Furthermore, under tensile-strain along the z-axis, the band gap of Li_3N becomes smaller so the onset of the hyperbolic region moves to lower energy and gets inside the visible region as described in Fig. 5. In addition, the hyperbolic windows are redshifted and become broader (narrower) in the visible (UV) region by increasing (decreasing) the lattice constant c. Inversely, under compressive strain, the spectral range of hyperbolicity moves to the UV region and becomes smaller due to the band gap increasing.

Having extensively explored the optical properties of Li_3N, we now investigate the possible existence of hyperbolicity in related alloys such as Li_2KN crystal structures. The lattice constants and internal coordinates of Li_2KN were fully optimized, and the obtained results ($a = b = 3.713$ and $c = 5.701$ Å) are completely consistent with the previous report [50]. Our calculations show that replacing a Li-ion on top of N with potassium (K) atoms reduces the interactions between the N-p_z and K-s orbitals, leading to the reversal of the band ordering between the conduction and valence bands at the center of the first BZ of Li_3N (see Fig. 6). In comparison to Li_3N, the spectral range of hyperbolicity is smaller and located below 6 eV in Li_2KN. In Li_2KN, the type-I hyperbolic frequency regime is broader than the type-II hyperbolic window with a hyperbolicity onset in the visible region at 2.3 eV, which is highly desirable in light device applications. The transition from type-I to type-II occurs at 2.79 eV, where $\mathrm{Re}\epsilon_{xx}$ and $\mathrm{Re}\epsilon_{zz}$ become zero with an opposite sign slope. The same scenario happens at 4.2 eV and type-II transforms into type-I indefinite permittivity media. The type-I hyperbolic frequency regime extends up to 5.3 eV. This interesting arrangement of various types of hyperbolic regimes makes Li_2KN an ideal tunable natural indefinite permittivity media where the type of hyperbolicity can be selected by tuning the energy of light. Furthermore, the loss function components show small values,

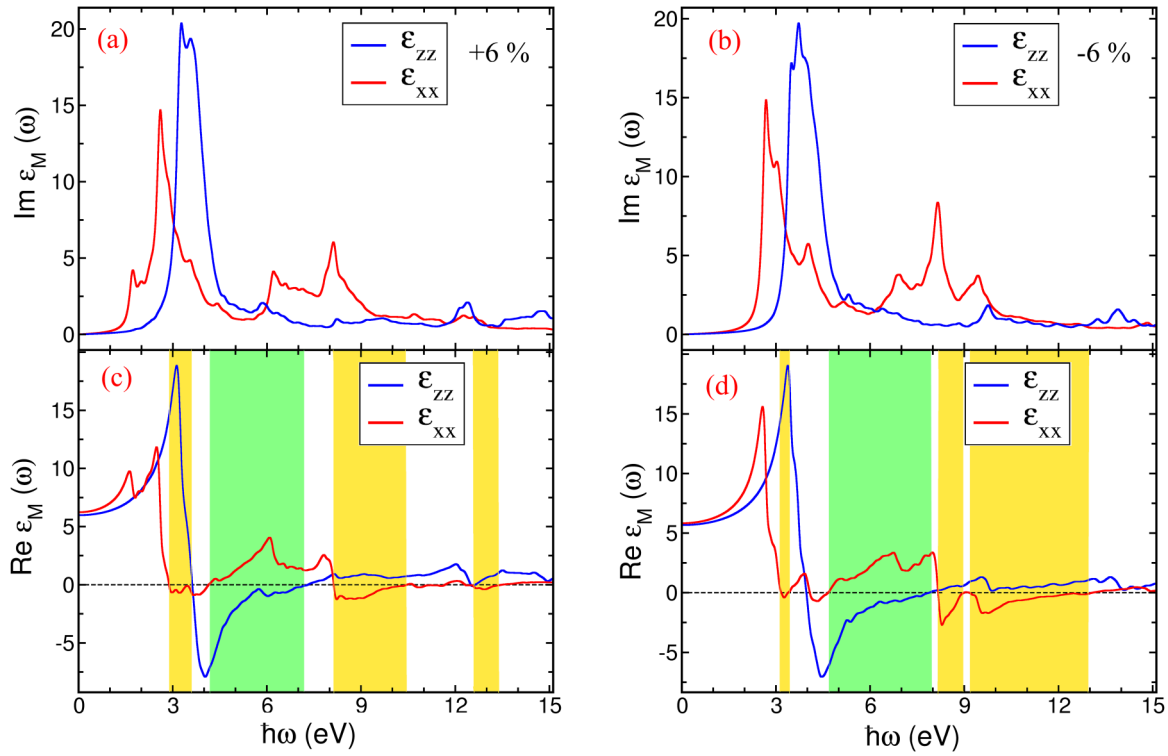

FIG. 5. The imaginary (a,b) and real parts (c,d) of the dielectric tensor to the in-plane (x-polarized) and out-of-plane (z-polarized) incident light for +6% (a,c) and −6%(b,d) strained Li_3N under tensile-strain along the z axis. The spectral regions for type-I and -II hyperbolicity are marked with a green and yellow background, respectively. The band gap becomes smaller in +6% strained Li_3N (a,c) so the onset of the hyperbolic region moves to lower energy and gets inside the visible region. In addition, the hyperbolic windows are redshifted and become broader (narrower) in the visible (UV) region by increasing (decreasing) the lattice constant c.

which means that there is almost no energy loss when the material is hyperbolic.

Finally, we consider the tunability of the optical properties of Li_3N by regulating its Fermi level with doping. We consider 0.1 holes per unit cell by setting the Fermi energy to 0.17 eV below the VBM (see Fig. 2). As the Fermi level crosses two valence bands perpendicular to the z-direction, an intense peak appears in $\mathrm{Im}\epsilon_{xx}$ at ∼0.1 eV (Fig. 7). In comparison to pristine Li_3N, under hole doping the x-polarized interband absorption above 2 and 6 eV becomes weaker and broader than the corresponding ones in pristine Li_3N. As a result, the negative values of the in-plane component of the real part of the dielectric function are less pronounced in hole-doped Li_3N causing the blueshift in type-II hyperbolic regimes. Our results show that the type-II hyperbolic frequency regime appears in the UV region (from 8.9 to 12.1). However, the main intense peak of $\mathrm{Im}\epsilon_{zz}$ is preserved and redshifted in hole-doped Li_3N. Therefore, the type-I hyperbolic frequency regime is located between 3.8 and 7.2 eV. The loss function of hole-doped Li_3N reflects perfectly the anisotropic electronic structures. Up to 5 eV the out-of-plane component of the loss function is nearly zero while the in-plane component has two small peaks. From 6 to 10 eV, the situation gets reversed and the out-of-plane component of the loss function exhibits a small peak in the vanishing region of the in-plane component. However, neglecting the peak around 7 eV, the loss function is negligible up to 11 eV.

IV. DISCUSSION AND CONCLUSION

Natural two-dimensional materials with anisotropic optical response are considered to be promising candidates for hosting a hyperbolic isofrequency surface. In addition, two-dimensional materials are characterized with highly confined and low-loss polaritons that can be additionally tuned with field effect techniques as well as with strain. In the present work, we provide a detailed *ab initio* study on an anisotropic optical response in hexagonal crystal structures. Using density functional theory and symmetry analysis, we have proposed α- and β-type hexagonal layered crystal structure as a new class of hyperbolic material where the hyperbolicity arises from weak Coulombic interactions between adjacent layers compared with interactions within a specific layer, in addition to symmetry constraints and transition selection rules. A comprehensive study of optical properties introduces this class of materials as a new natural hyperbolic material in which the type of hyperbolicity can be selected by changing the frequency of light. More excitingly, the hyperbolicity in these materials can be tuned using lattice strain along the z-axis and doping as well. Furthermore, the many-body effects on the dielectric functions are discussed. We have also shown that this class of materials are a low loss in hyperbolic frequency regimes, making them ideal natural hyperbolic materials. Our findings here can be explored by current experiments.

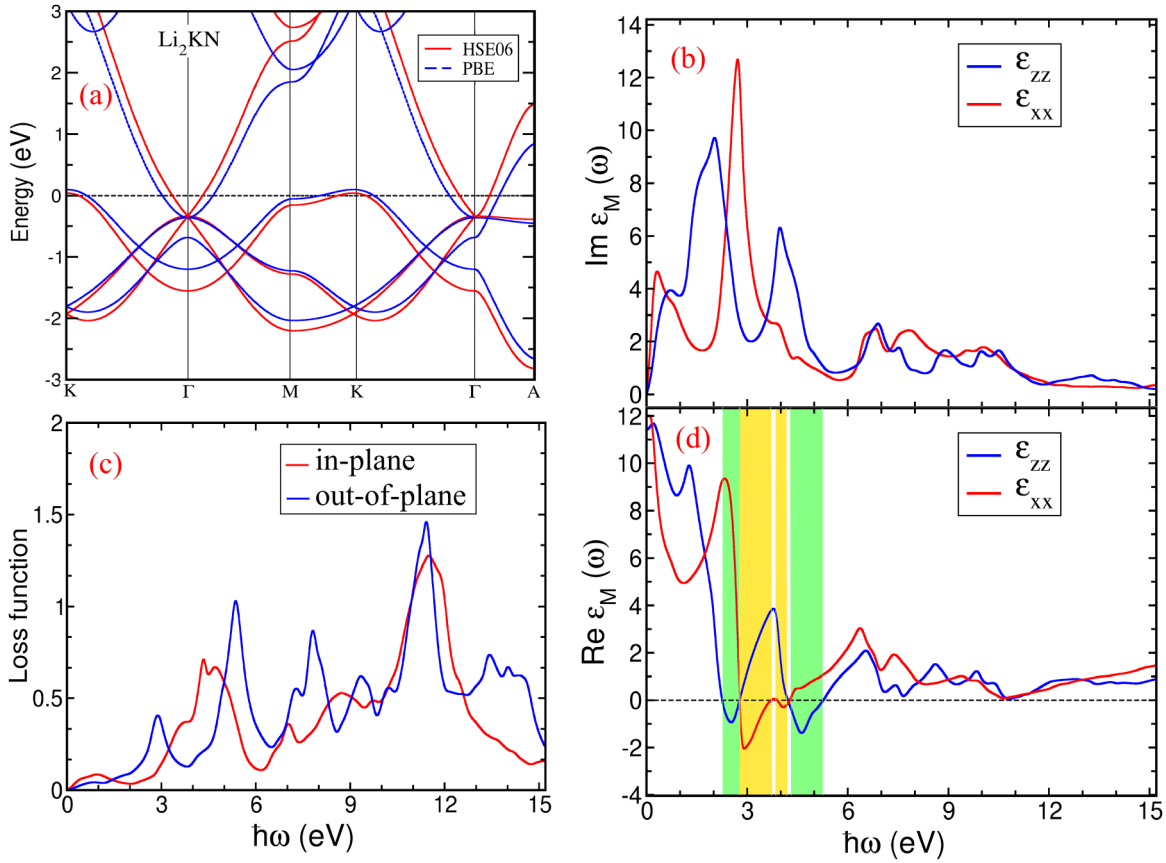

FIG. 6. (a) The calculated bulk electronic band structure and (c) the energy loss function to the in-plane (x-polarized) and out-of-plane (z-polarized) incident light for Li_2KN. (b) The imaginary and (d) real parts of the dielectric tensor to the in-plane (x-polarized) and out-of-plane (z-polarized) incident light for Li_2KN. The spectral regions for type-I and -II hyperbolicity are marked with a green and yellow background, respectively. The type-I hyperbolic frequency regime is broader than the type-II hyperbolic window with a hyperbolicity onset in the visible region at 2.3 eV. The transition from type I to type II occurs at 2.79 eV, where $\mathrm{Re}\epsilon_{xx}(\omega)$ and $\mathrm{Re}\epsilon_{zz}(\omega)$ vanish with an opposite sign slope. Furthermore, the loss function components show small values, meaning that there is no energy loss when the material is hyperbolic.

Ultimately, we would like to emphasize potential viable applications of α- (β-) type hexagonal layered crystal structures in comparison with layered transition metal dichalcogenides (TMDs) [51]. First of all, as discussed in this paper, this new class of hyperbolic materials exhibits both type-I and type-II hyperbolicity over the wide range of frequencies rarely found in nature [51]. As a result, the type of hyperbolicity can be selected by tuning the energy of light.

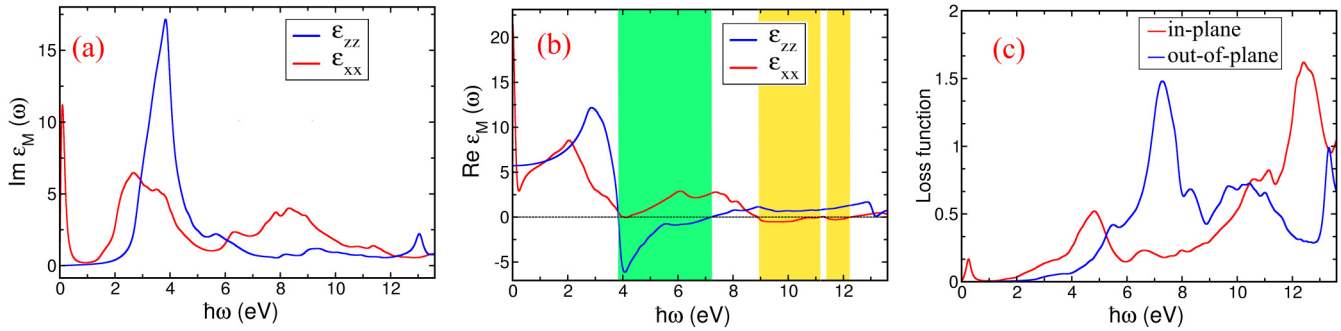

FIG. 7. (a) The imaginary and (b) real parts of the dielectric tensor to the in-plane (x-polarized) and out-of-plane (z-polarized) incident light for hole-doped (0.1 holes/u.c.) Li_3N. The spectral regions for type-I and -II hyperbolicity are marked with a green and yellow background, respectively. (c) The energy loss function for in-plane and out-of-plane incident light. Under hole doping, the x-polarized interband absorption above 2 and 6 eV becomes weaker and broader than corresponding ones in pristine Li_3N. The negative values of the in-plane component of the real part of the dielectric function are less pronounced in hole-doped Li_3N. The loss function reflects the anisotropic electronic structures. Up to 5 eV, the out-of-plane component of the loss function is nearly zero while the in-plane component contains two low intensity peaks.

Secondly, a previous study showed that the low losses, which are mainly responsible for the large Purcell factor in the hyperbolicity regime, only meet at the metallic TMDs where the conduction bands are sufficiently separated from other bands by finite energy band gaps. However, our calculations show that α- (β-) type crystal structures, both metallic and semiconductor, are nearly lossless in the hyperbolic windows. Most importantly, in α- (β-) type crystal structures, the impressive dependency of the conduction band on the lattice constant c provides the hyperbolicity tunability in these hexagonal structures under strain, doping, and alloying, which are more plausible than heterostructures of standard TMDs.

ACKNOWLEDGMENTS

A.E. is supported by Iran Science Elites Federation and R.A. is supported by the Australian Research Council Centre of Excellence in Future Low-Energy Electronics Technologies (Project No. CE170100039).

[1] A. Poddubny, I. Iorsh, P. Belov, and Y. Kivshar, Nat. Photon. **7**, 948 (2013).
[2] A. J. Hoffman, L. Alekseyev, S. S. Howard, K. J. Franz, D. Wasserman, V. A. Podolskiy, E. E. Narimanov, D. L. Sivco, and C. Gmachl, Nat. Mater. **6**, 946 (2007).
[3] J. Yao, Z. Liu, Y. Liu, Y. Wang, C. Sun, G. Bartal, A. M. Stacy, and X. Zhang, Science **321**, 930 (2008).
[4] Z. Liu, H. Lee, Y. Xiong, C. Sun, and X. Zhang, Science **315**, 1686 (2007).
[5] J. Rho, Z. Ye, Y. Xiong, X. Yin, Z. Liu, H. Choi, G. Bartal, and X. Zhang, Nat. Commun. **1**, 143 (2010).
[6] W. T. Lu and S. Sridhar, Phys. Rev. B **77**, 233101 (2008).
[7] J. Yao, X. Yang, X. Yin, G. Bartal, and X. Zhang, Proc. Natl. Acad. Sci. (USA) **108**, 11327 (2011).
[8] X. Yang, J. Yao, J. Rho, X. Yin, and X. Zhang, Nat. Photon. **6**, 450 (2012).
[9] J. Sun, N. M. Litchinitser, and J. Zhou, ACS Photon. **1**, 293 (2014).
[10] S. Guan, S. Y. Huang, Y. Yao, and S. A. Yang, Phys. Rev. B **95**, 165436 (2017).
[11] W. Ma, P. Alonso-González, S. Li, A. Y. Nikitin, J. Yuan, J. Martín-Sánchez, J. Taboada-Gutiérrez, I. Amenabar, P. Li, S. Vélez, *et al.*, Nature (London) **562**, 557 (2018).
[12] P. Li, I. Dolado, F. J. Alfaro-Mozaz, F. Casanova, L. E. Hueso, S. Liu, J. H. Edgar, A. Y. Nikitin, S. Vélez, and R. Hillenbrand, Science **359**, 892 (2018).
[13] Z. Zheng, N. Xu, S. L. Oscurato, M. Tamagnone, F. Sun, Y. Jiang, Y. Ke, J. Chen, W. Huang, W. L. Wilson, *et al.*, Sci. Adv. **5**, eaav8690 (2019).
[14] S. Edalati-Boostan, C. Cocchi, and C. Draxl, Phys. Rev. Mater. **4**, 085202 (2020).
[15] J. Sun, J. Zhou, B. Li, and F. Kang, Appl. Phys. Lett. **98**, 101901 (2011).
[16] L. V. Alekseyev, V. A. Podolskiy, and E. E. Narimanov, Adv. OptoElectron. **2012**, 267564 (2012).
[17] M. Esslinger, R. Vogelgesang, N. Talebi, W. Khunsin, P. Gehring, S. De Zuani, B. Gompf, and K. Kern, Acs Photon. **1**, 1285 (2014).
[18] K. Korzeb, M. Gajc, and D. A. Pawlak, Opt. Express **23**, 25406 (2015).
[19] C. Wang, S. Huang, Q. Xing, Y. Xie, C. Song, F. Wang, and H. Yan, Nat. Commun. **11**, 1 (2020).
[20] D. N. Basov, M. M. Fogler, and F. J. García de Abajo, Science **354**, 6309 (2016).
[21] T. Low, A. Chaves, J. D. Caldwell, A. Kumar, N. X. Fang, P. Avouris, T. F. Heinz, F. Guinea, L. Martin-Moreno, and F. Koppens, Nat. Mater. **16**, 182 (2017).
[22] E. E. Narimanov and A. V. Kildishev, Nat. Photon. **9**, 214 (2015).
[23] A. Ebrahimian, R. Asgari, and M. Dadsetani, Phys. Rev. B **102**, 165119 (2020).
[24] I. Loa, K. Kunc, K. Syassen, and P. Bouvier, Phys. Rev. B **66**, 134101 (2002).
[25] C. Cheng, M.-Y. Duan, Z. Wang, and X.-L. Zhou, Philos. Mag.1 (2020).
[26] T. Nie, L. Meng, Y. Li, Y. Luan, and J. Yu, J. Phys.: Condens. Matter **30**, 125502 (2018).
[27] L. Jin, X. Zhang, T. He, W. Meng, X. Dai, and G. Liu, Phys. Chem. Chem. Phys. **22**, 5847 (2020).
[28] See the supplemental material at http://link.aps.org/supplemental/10.1103/PhysRevB.103.035425 for the electronic band structure and optical responses of several members of materials with hexagonal $P6/mmm$ and $P6_3/mmc$ layered crystal structures.
[29] A. Gulans, S. Kontur, C. Meisenbichler, D. Nabok, P. Pavone, S. Rigamonti, S. Sagmeister, U. Werner, and C. Draxl, J. Phys.: Condens. Matter **26**, 363202 (2014).
[30] J. Heyd, G. E. Scuseria, and M. Ernzerhof, J. Chem. Phys. **118**, 8207 (2003).
[31] K. Hummer, J. Harl, and G. Kresse, Phys. Rev. B **80**, 115205 (2009).
[32] J. P. Perdew, K. Burke, and M. Ernzerhof, Phys. Rev. Lett. **77**, 3865 (1996).
[33] Z. Nourbakhsh and R. Asgari, Phys. Rev. B **94**, 035437 (2016).
[34] W. Hanke and L. J. Sham, Phys. Rev. B **38**, 13361 (1988).
[35] G. Strinati, La Rivista del Nuovo Cimento (1978-1999) **11**, 1 (1988).
[36] G. Onida, L. Reining, and A. Rubio, Rev. Mod. Phys. **74**, 601 (2002).
[37] P. Puschnig and C. Ambrosch-Draxl, Phys. Rev. B **66**, 165105 (2002).
[38] M. Rohlfing and S. G. Louie, Phys. Rev. B **62**, 4927 (2000).
[39] M. Dadsetani and A. Ebrahimian, J. Phys. Chem. Solids **100**, 161 (2017).
[40] M. Dadsetani, A. Ebrahimian, and H. Nejatipour, Mater. Sci. Semicond. Proc. **34**, 236 (2015).
[41] E. K. U. Gross and W. Kohn, Phys. Rev. Lett. **55**, 2850 (1985).
[42] J. Yan, J. J. Mortensen, K. W. Jacobsen, and K. S. Thygesen, Phys. Rev. B **83**, 245122 (2011).
[43] G. Nazri, C. Julien, and H. Mavi, Solid State Ion. **70**, 137 (1994).
[44] H. J. Beister, S. Haag, R. Kniep, K. Strössner, and K. Syassen, Angew. Chem., Int. Ed. Engl. **27**, 1101 (1988).

[45] G. V. Vajenine, X. Wang, I. Efthimiopoulos, S. Karmakar, K. Syassen, and M. Hanfland, Phys. Rev. B **79**, 224107 (2009).
[46] S. Hotta, *Mathematical Physical Chemistry* (Springer, Berlin, 2018).
[47] D. Korobkin, B. Neuner, C. Fietz, N. Jegenyes, G. Ferro, and G. Shvets, Opt. Express **18**, 22734 (2010).
[48] J. Singh, *Optical Properties of Condensed Matter and Applications* (Wiley, New York, 2006), Vol. 6.
[49] H. Wang and T. Low, Phys. Rev. B **102**, 241104(R) (2020).
[50] J. Schön, M. Wevers, and M. Jansen, Solid State Sci. **2**, 449 (2000).
[51] M. N. Gjerding, R. Petersen, T. G. Pedersen, N. A. Mortensen, and K. S. Thygesen, Nat. Commun. **8**, 1 (2017).